

## Measuring distributions of diffusivity in turbulent fluids with magnetic-resonance imaging

Dean O. Kuethe

*Department of Radiology, Box 3808, Duke University Medical Center, Durham, North Carolina 27710*

(Received 17 April 1989)

This paper describes a method for measuring distributions of turbulent diffusivity in less than an hour. The measurement is rapid enough to aid in designing devices that make use of the turbulent diffusion of mass, heat, or momentum. It may be useful as a measurement of the degree of turbulence in the blood of patients with cardiovascular diseases. It consists of subtracting the natural logarithms of the pixel values of a magnetic-resonance image of turbulent fluid from those of stationary fluid. The pixel values of the resulting image are multiplied by a constant to yield diffusivities. The accuracy of the measurement is within the range of diffusivities (1) upstream as far as the speed of the fluid multiplied by the time  $T_E$  between exciting the spin system and recording the signal, (2) in the direction of the gradient of diffusivity as far as  $T_E$  multiplied by 5 times the gradient of the diffusivity, and (3) in the direction of the phase-encoding magnetic field gradient as far as the negative of the component of velocity in the phase-encoding direction multiplied by the time between phase encoding and recording the signal. In a  $32 \times 32$ -cm<sup>2</sup> image of a jet of water with a nozzle velocity of  $4.5 \text{ m s}^{-1}$  and Reynolds number of 18 000, made with a  $T_E$  of 15 ms, the distance of (1) ranged from 0 to 6.7 cm, of (2) ranged from 0 to 0.3 cm, and of (3) ranged from 0 to 0.4 cm. These distances are bounds; the actual spatial misregistration was less. The signal-to-noise ratio ranged from 10 to 15 for diffusivities from  $0.02$  to  $0.7 \text{ cm}^2 \text{ s}^{-1}$ .

### I. INTRODUCTION

Substances dissolved in turbulent fluids tend to diffuse with dynamics similar to those of molecular diffusion, only faster. Measuring the distribution of diffusivity in turbulent fluids has been difficult; for example, it can take months to tabulate the diffusivities for a large array of points when the velocity probability distributions are measured with laser Doppler anemometry. This paper presents a method by which the measurement can be accomplished in less than an hour. The theory used is similar to that for measuring molecular diffusivities with magnetic resonance.<sup>1</sup> Some sources of errors in imaging turbulent diffusivities discussed in this paper should be applicable to imaging distributions of molecular diffusivity.<sup>2</sup>

To model the dispersion of substances in turbulent fluids as a diffusion, the velocity  $\mathbf{v}$  at a point is defined as the sum of a steady component  $\mathbf{v}_0$  and a random component  $\mathbf{V}$ :  $\mathbf{v} = \mathbf{v}_0 + \mathbf{V}$ . If according to the random component  $\mathbf{V}$ , in a given time period, a particle is equally likely to travel a given distance in any direction,<sup>3</sup> then, on the average, substances will diffuse from higher concentration to lower according to  $\mathbf{Q} = -D\nabla c$ , where  $\mathbf{Q}$  is the flux density of substance,  $D$  is the diffusivity, and  $c$  is the concentration. By the conservation of mass,  $c$  will obey the diffusion equation,<sup>4</sup>

$$\frac{\partial c}{\partial t} = -\nabla \cdot (\mathbf{v}_0 c) + \nabla \cdot (D \nabla c). \quad (1)$$

While characterizing the degree of turbulence with a diffusivity is a simplified model of fluid behavior, it has proven valuable for predicting how pollutants disperse in

water and air,<sup>5</sup> and modeling how animals communicate with chemical signals.<sup>6</sup> It has been applied to a limited set of man-made devices<sup>7</sup> but has not been used extensively in developing products because of the time involved in measuring distributions of  $D$ .

Measurements of turbulent diffusivity may help in engineering carburetors, heat exchangers, low-drag car bodies, etc., devices that make use of the turbulent diffusion of mass, heat, or momentum. In medicine, measuring diffusivities of turbulent blood flow may help determine the severity of cardiovascular diseases.

One method of establishing that the diffusion equation (1) can be applied to a given flow is based on a theory of Batchelor.<sup>8</sup> He predicted that the measured  $D$  would increase in proportion to observation time (time of flight) from zero and eventually reach an asymptotic value. With magnetic-resonance imaging, the observation time is well defined as the echo time  $T_E$ , the time between exciting the spin system and recording the signal. If for a given flow, the measured  $D$ 's reach an asymptote at an echo time  $T_{E_a}$ , then, if an application does not require resolving time in increments less than  $T_{E_a}$ , the diffusion equation will be an adequate model for the average concentration of substances.

In this paper distributions of  $D$  are measured in water with magnetic-resonance imaging for a turbulent jet and turbulent pipe flow at different Reynolds numbers using six different  $T_E$ 's. The method requires making two images, one of stationary water, one of moving water. An image is a  $256 \times 256$  array of numbers (pixel values), each representing a region of space, which can be used for calculations or displayed as black, white, or shades of gray on a video screen. The pixel values of the two images are

used to calculate an image whose pixel values are diffusivities for each of the  $256^2$  regions.

Distributions for  $D$  in fluids other than water can be calculated using dynamic similarity. For instance, one could predict the diffusivities of air in a carburetor by measuring the diffusivities in a model of the carburetor with water flowing through it at the same Reynolds number.<sup>9</sup>

One of the difficulties in developing the measurement technique was determining what its errors are. Bounds for the errors are derived in the Appendix.

## II. METHODS AND MATERIALS

### A. Rationale for the method

An assemblage of hydrogen nuclei in a magnetic field with flux density  $\mathbf{B}$  will interact with electromagnetic radiation at the resonance frequency  $\omega/2\pi$ , where  $\omega = \gamma|\mathbf{B}|$ , and  $\gamma$  is the gyromagnetic ratio  $2.675 \times 10^8 \text{ T}^{-1} \text{ s}^{-1}$ . For the 1.5-T magnet used in this study  $\omega/2\pi$  is 63.91 MHz, a radio frequency. After a brief pulse of radio waves, oriented with their magnetic moment perpendicular to  $\mathbf{B}$ , the assemblage will have a magnetic moment perpendicular to  $\mathbf{B}$  that rotates with frequency  $\omega/2\pi$ . This "transverse magnetization" is represented by a complex moment density  $m(\mathbf{x}, t)$ , a function of space and time, that satisfies<sup>10</sup>

$$\frac{\partial m}{\partial t} = -i\omega_0 m - i\gamma \mathbf{x} \cdot \mathbf{G} m - \frac{m}{T_2^*} - \nabla(\mathbf{v}_0 m) + \nabla(D \nabla m), \quad (2)$$

where  $i = \sqrt{-1}$ , and  $\omega_0$  is the angular velocity of  $m$  in the primary field of flux density  $\mathbf{B}_0$ . The flux density may be altered by an experimentally imposed gradient  $\mathbf{G}$  in the magnetic field such that  $|\mathbf{B}| = |\mathbf{B}_0| + \mathbf{x} \cdot \mathbf{G}$ , where  $\mathbf{x}$  is the position in space. By convention  $\mathbf{B}$  and  $\mathbf{B}_0$  point in the positive  $z$  direction.  $T_2^*$  is a time constant for an exponential decay. The first term on the right-hand side indicates that  $m$  rotates at a primary frequency  $\omega_0/2\pi$ ; the second describes how the phase of  $m$  changes as it rotates faster or slower by being at different field strengths as a result of position in an imposed magnetic gradient; the third models with an exponential decay the decrease in magnitude of  $m$  caused by a theoretical exponential decay (time constant  $T_2$  in Ref. 11), molecular diffusion, and unintentional gradients in the magnetic field;<sup>12</sup> the fourth and fifth term describes the diffusion of magnetic moments in a turbulent fluid [compare with (1)].

For the case where  $D$  is a constant and there are no boundaries.

$$m = \exp \left[ -i\omega_0 t - \frac{t}{T_2^*} - i\gamma \mathbf{x} \cdot \int_0^t \mathbf{G}(t') dt' + i\gamma \mathbf{v}_0 \cdot \int_0^t \int_0^{t'} \mathbf{G}(t'') dt'' dt' - \gamma^2 D U(t) \right], \quad (3)$$

where

$$U(t) = \int_0^t \left[ \int_0^{t'} \mathbf{G}(t'') dt'' \right] \cdot \left[ \int_0^{t'} \mathbf{G}(t'') dt'' \right] dt'$$

is a solution to (2) satisfying the initial condition,  $m(\mathbf{x}, 0) = 1 + 0i$ , assuming no additional radio waves are transmitted.<sup>13</sup> [We are employing the conservation of mass equation,  $\nabla \mathbf{v}_0 = 0$  (Ref. 9).] The first three terms of the exponent contain neither  $\mathbf{v}_0$  nor  $D$  and would be the same for either stationary or moving fluid. It is possible to impose the gradient  $\mathbf{G}$  so that at a specified time  $T_E$ ,  $\int_0^{T_E} \int_0^{t'} \mathbf{G}(t'') dt'' dt' = (0, 0, 0)$  (Ref. 14). Then, at  $T_E$ , the only difference between  $m$  in (3) for stationary and moving fluid would be a factor of  $\exp[-\gamma^2 D U(T_E)]$  ( $D$  is zero for stationary fluid).

Ideally, each of the pixel values of an image is the magnitude of the average of  $m$  in the region represented by the pixel at  $T_E$ . So if (3) is assumed a correct representation of  $m$  and we multiply the difference between the natural logarithms of the pixel values of the image of stationary fluid and the natural logarithms of the pixel values of the image of moving fluid by  $1/[\gamma^2 U(T_E)]$ , the resulting image will have pixel values of  $D$ :

$$D(\mathbf{x}) = \frac{\ln[m_s(\mathbf{x}, T_E)] - \ln[m_m(\mathbf{x}, T_E)]}{\gamma^2 U(T_E)}, \quad (4)$$

where the subscripts  $s$  and  $m$  stand for stationary and moving fluid, respectively.

However, (3) is not an accurate representation of  $m$  because  $D$  was assumed to be a constant to obtain it. Also, the data for constructing an image are not collected at only one point in time  $T_E$ , but over an interval of time surrounding  $T_E$ , and  $\int_0^{T_E} \int_0^{t'} \mathbf{G}(t'') dt'' dt' \neq (0, 0, 0)$  over that entire interval. The errors caused by these false assumptions are analyzed in the Appendix. The bias can be summarized as a lack of spatial resolution by stating the following: A diffusivity at a point in the image represents a diffusivity somewhere in the region within  $|T_E [D \gamma^2 U(T_E)] \nabla D|$  in the direction of either  $\pm \nabla D$ , and within  $|T_E \mathbf{v}_0|$  upstream, and within  $-v_{0y} \Delta t$  in the  $y$  direction [ $\Delta t$  is the time from the centroid of  $\int_0^{T_E} G_y(t') dt$  to  $T_E$ ;  $y$  is the phase encoding (see Sec. II C 3) direction]. There will also be a reduction in the signal-to-noise ratio.

The simplification of including the signal decay from the  $T_2$  process of Bloch<sup>11</sup> and molecular diffusion in the imposed gradient in a single decay process with time constant  $T_2^*$  will not cause errors in the method, because if a separate term had been included in (2) for molecular diffusion, it would produce a term in the solution that would be the same for stationary and moving fluid. On the other hand, including signal decay from turbulent diffusion in unintentional gradients in the  $T_2^*$  process will cause errors. In effect,  $1/[\gamma^2 U(T_E)]$  will be overestimated so  $D$  will be overestimated. The error can be determined from the possible inhomogeneity of the primary field (see Sec. II D).

### B. Signal-to-noise estimates

Rather than calculate a theoretical contribution from every source of noise, estimates of the signal to noise

were obtained from final images of  $D$ . Two images of  $D$  were produced (from two independent sets of images of stationary and moving water) and subtracted to produce a difference image.

The signal-to-noise ratio for a region (a group of neighboring pixels) was calculated as the mean of the pixels of a  $D$  image times  $\sqrt{2}$  divided by the standard deviation of the pixels in the difference image.

### C. How images are made: A brief description of two-dimensional Fourier-transform imaging (Ref. 15)

#### 1. Slice selecting

Discrimination in one spatial dimension  $z$  is achieved by exciting only the hydrogen nuclei between two parallel planes. A gradient in the magnetic field in the  $z$  direction  $\mathbf{G}=(0,0,G_z)$  is imposed so that the resonance frequency  $\omega/2\pi$  is a linear function of  $z$ :  $\omega=\gamma|\mathbf{B}_0|+zG_z$ . The radio waves are broadcast between frequencies  $\gamma(|\mathbf{B}_0|+z_1G_z)/2\pi$  and  $\gamma(|\mathbf{B}_0|+z_2G_z)/2\pi$  so that only nuclei between  $z_1$  and  $z_2$  are excited.

#### 2. Frequency encoding

To discriminate a second dimension  $x$ , a gradient in the magnetic field  $(G_x,0,0)$  is imposed while the data are being collected. This makes the frequency of transverse magnetization  $\omega/2\pi$  a linear function of  $x$ :  $\omega=\gamma|\mathbf{B}_0|+xG_x$ . Because the frequency of different regions is different, their phase changes relative to each other. If the phase began as a constant function of  $x$ , the signal would decrease during data collection as regions became out of phase. Rather, before data collection, a gradient is imposed of the opposite sign in the  $x$  direction so that the regions begin out of phase, realign to give the greatest signal magnitude at the echo time  $T_E$ , and then dephase again. Assuming  $m$  in all regions lies along the real axis at  $T_E$ , the resulting signal  $S$  is  $e^{-i\omega_0(t-T_E)}$  times the Fourier transform of the distribution of transverse magnetization in  $x$ :

$$S(t)=S(\alpha)=e^{-i\omega_0(t-T_E)}\int_{-\infty}^{\infty}e^{-i\alpha s_x}M ds_x, \quad (5)$$

where  $M=me^{+i\omega_0(t-T_E)+i\gamma x G_x(t-T_E)}$ ;  $\alpha=\gamma\xi G_x(t-T_E)$ , where  $\xi$  is the field of view of the image; and  $s_x=x/\xi$ . The signal is recorded digitally at 256 equally spaced times.

#### 3. Phase encoding

To discriminate in the third spatial dimension  $y$ , data are collected from 256 different excitations. Before each data collection, a gradient  $(0,G_y,0)$  is imposed for a given time interval  $t_1$  to  $t_2$ . This makes the phase of the transverse magnetization a linear function of  $y$ . It reduces the signal received by putting regions out of phase with each other.  $G_y$  has a different value before each data collection so that the signal as a function of excitation number  $k$  is  $e^{-i\omega_0(t-T_E)}$  times the Fourier transform of the distribution of transverse magnetization in  $y$ :

$$S(\beta_k)=e^{-i\omega_0(t-T_E)}\int_{-\infty}^{\infty}e^{-i\beta_k s_y}M ds_y, \quad (6)$$

where  $\beta_k=\gamma\xi\int_{t_1}^{t_2}G_y(t')dt'$  ranges from  $-254\pi$  to  $256\pi$  in steps of  $2\pi$  as  $G_y$  is incremented, and  $s_y=y/\xi$ .

#### 4. The image

For each of the 256 values of  $\beta_k$ , 256 values of  $S(\alpha)$  are recorded. One complete set of data  $S(\alpha,\beta)$  contains  $256^2$  complex numbers. To make an image, a discrete two-dimensional inverse Fourier transform of the recorded data is taken:

$$f(s_x,s_y)=\sum_{j=0}^{N-1}\sum_{k=0}^{N-1}F(\alpha,\beta)e^{i2\pi j s_x+i2\pi k s_y}$$

$$\text{for } \alpha = \begin{cases} j2\pi, & j=0,1,\dots,N/2-1 \\ (j-N)2\pi, & j=N/2,\dots,N-1 \end{cases}$$

and

$$\beta = \begin{cases} k2\pi, & k=0,1,\dots,N/2-1 \\ (k-N)2\pi, & k=N/2,\dots,N-1 \end{cases} \quad (7)$$

where  $F(\alpha,\beta)=S(\alpha,\beta)e^{+i\omega_0(t-T_E)}$  and

$s_x$  and  $s_y$  range over

$$\begin{cases} n/N, & n=0,1,\dots,N/2-1 \\ (n-N)/N, & n=N/2,\dots,N-1 \end{cases}$$

The image is the magnitude of  $f$ .

#### D. Imager

A clinical Signa<sup>®</sup>, GE Corporation, Milwaukee, 1.5-T magnetic-resonance imager with shielded gradient coils was used. Inhomogeneities in the  $\mathbf{B}_0$  field were maintained to within 20 Hz over a 20-cm-diam cylinder of water. The pulse sequence, a gradient refocused echo sequence [GRASS (GE), only one  $\pi/2$  radio wave pulse is used] that can be moment nulled so that  $\int_0^{T_E}tG_x(t')dt'=0$  and  $\int_0^{T_E}t'G_z(t')dt'=0$  (Ref. 14) was modified so that the  $G_y$  gradient was executed as close as possible to acquiring data with the  $G_x$  gradient (Fig. 1). The imposed gradients were known to within  $\pm 0.01$  G/cm, the timing was known to within  $\pm 0.1$   $\mu$ s. The pulse sequence was repeated every 0.5 s. The  $T_1$  relaxation time constant<sup>11</sup> of the water with  $(10^{-3}\pm 10^{-5})M$  GdCl<sub>3</sub> EDTA (ethylenediamine tetra-acetic acid) was  $130\pm 10$  ms (3.8 times shorter than the repetition time). Water that had been previously excited produced at least 98% of the signal of water that might enter the slice having never been excited. A 1-cm-thick slice was excited, the field of view  $\xi$  was either 32 or 24 cm. Each image was made from the average of two complete sets of data; the acquisition time was 4 min 23 s.

The values of  $1/[\gamma^2 U(T_E)]$  for the pulse sequence (Fig. 1) using a 32-cm field of view were 0.169, 0.184, 0.220, 0.240, 0.246, and 0.248  $\text{cm}^2\text{s}^{-1}$  for echo times of 13, 15, 25, 50, 75, and 100 ms, respectively. For a 24-cm field of view, the values for the same echo times were

0.098, 0.107, 0.130, 0.142, 0.145, and 0.147  $\text{cm}^2 \text{s}^{-1}$ . The  $y$  gradient was assumed to be  $\frac{1}{2}$  the maximum of its 256 values. As an example of how the directions were weighted, for a 32-cm field of view and a 13-ms echo time (Fig. 1), the  $x$  gradient accounted for 73.6% of  $U(T_E)$ ; the  $y$  gradient, 14.4%; the  $z$  gradient, 12.0%. Unintentional gradients would have to have been 50 times greater than the  $B_0$  inhomogeneity before omitting them from the calculations would bias the measurement of  $D$  by 1%.

### E. Flow apparatuses

#### 1. Jet

The jet from a  $4 \pm 0.1$  mm Lucite<sup>®</sup> tube  $217 \pm 1$  mm long flowed into the center of one flat wall of a Lucite right circular cylinder  $214 \pm 2$  mm in diameter and  $643 \pm 1$  mm long. The opposite wall was drained by a  $12 \pm 1$ -mm-diam Lucite tube. The tube ends were flush with the cylinder walls. A constant flow rate of water with  $(10^{-3} \pm 10^{-5})M$   $\text{GdCl}_3$  EDTA was produced by gravity feed with an overflowing head tank  $4 \pm 0.5$  m high. Steady flow rates, 0, 25.5, 35.6, 46.9, and  $56.7 \text{ cm}^3 \text{ s}^{-1}$  were measured to within  $\pm 0.2 \text{ cm}^3 \text{ s}^{-1}$ . The maximum

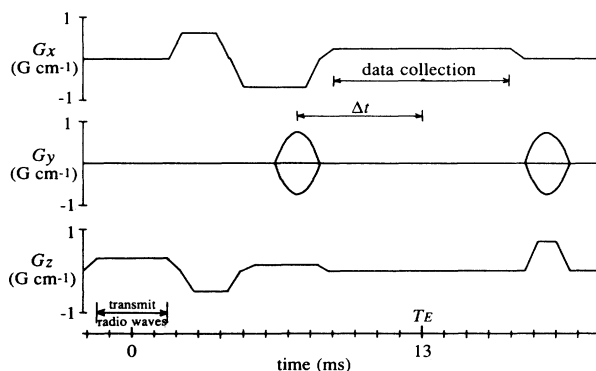


FIG. 1. Pulse sequence. Graphs show the timing of the three components  $G_x$ ,  $G_y$ , and  $G_z$  of the imposed magnetic field gradient  $\mathbf{G}$  for a 32-cm field of view and a 13-ms echo time. A gradient in the  $z$  direction ensures that only a slice of fluid is excited while the radio waves are transmitted. A phase-encoding gradient in the  $y$  direction is incremented through 256 different strengths (the maximum, minimum, and zero are shown) before data collection for each of the 256 repetitions of the sequence. A gradient in the  $x$  direction provides frequency encoding during the data collection period surrounding the echo time  $T_E$ . The pulse sequence is designed so that  $T_E \int_0^{T_E} G_y(t') dt' - \int_0^{T_E} t' G_y(t') dt'$  is minimized by minimizing  $\Delta t$ , and  $\int_0^{T_E} G_x(t') dt' = \int_0^{T_E} t' G_x(t') dt' = \int_0^{T_E} G_z(t') dt' = \int_0^{T_E} t' G_z(t') dt' = 0$ . The extra gradients after data collection in the  $x$  and  $z$  directions are for rephasing and dephasing material in preparation for the subsequent excitation; they are part of the present sequence of use when the repetition time is much shorter than that used in the present study.

velocity in the tube was below  $5 \text{ m s}^{-1}$  so that with a  $T_E$  of 25 ms, if 12.5 cm of the tube was in the image, no water entered the jet without having been excited. The jet was imaged at echo times of 13, 15, and 25 ms with a 32-cm field of view.

#### 2. Pipe flow

A  $9.5 \pm 0.1$ -mm-diam Lucite pipe with an entrance length of 50 diameters was supplied with a constant flow rate of 0, 82, 134, and  $220 \pm 1.5 \text{ cm}^3 \text{ s}^{-1}$ . It was imaged at echo times of 13, 15, 25, 50, 75, and 100 ms at both a 24- and 32-cm field of view. For both types of flow, the water spent at least ten times  $T_1$  at 1.5 T before entering the apparatus so it was fully magnetized.

### III. RESULTS

Figure 2 shows contour maps of the diffusivity of the turbulent jet at four different flow rates measured at a  $T_E$  of 13 ms. The contour maps are produced by choosing a series of evenly spaced diffusivity values, 0.02, 0.08, . . . , 0.50,  $0.56 \text{ cm}^2 \text{ s}^{-1}$ . For each value, the image is displayed so that the pixels above that value are white, below it are black (Fig. 3). Each contour line of

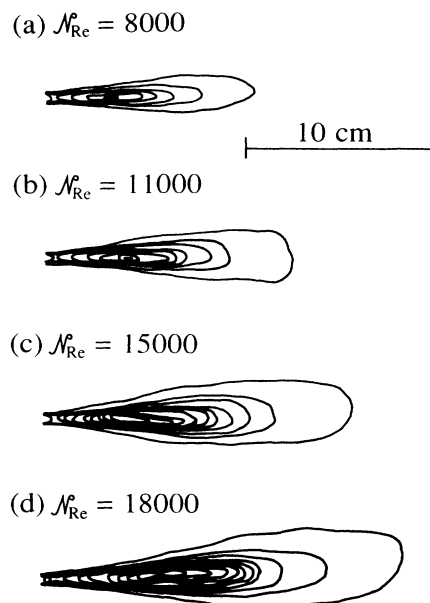


FIG. 2. Contour maps of diffusivity in four different speed jets. (a) Reynolds number  $\mathcal{N}_{Re}$  is 8000.  $\mathcal{N}_{Re} = \rho L \bar{v} / \eta$ , where  $\rho$  is the density of water ( $1000 \text{ kg m}^{-3}$ ),  $L$  is the diameter of the nozzle (0.0040 m),  $\eta$  is the viscosity of the water ( $0.0010 \text{ kg m}^{-1} \text{ s}^{-1}$ ),  $\bar{v} = 2.02 \text{ m s}^{-1}$  is the flow rate  $2.55 \times 10^{-5} \text{ m}^3 \text{ s}^{-1}$  divided by the nozzle area  $1.26 \times 10^{-5} \text{ m}^2$ . (b)  $\mathcal{N}_{Re} = 11000$ ,  $\bar{v} = 2.90 \text{ m s}^{-1}$ . (c)  $\mathcal{N}_{Re} = 15000$ ,  $\bar{v} = 3.73 \text{ m s}^{-1}$ . (d)  $\mathcal{N}_{Re} = 18000$ ,  $\bar{v} = 4.51 \text{ m s}^{-1}$ . Contour lines are at 0.02, 0.08, 0.14, 0.20, 0.26, 0.32, 0.38, 0.44, 0.50, and  $0.56 \text{ cm}^2 \text{ s}^{-1}$ . The frequency-encoding direction is left to right, the phase-encoding direction is bottom to top, the echo time is 13 ms.

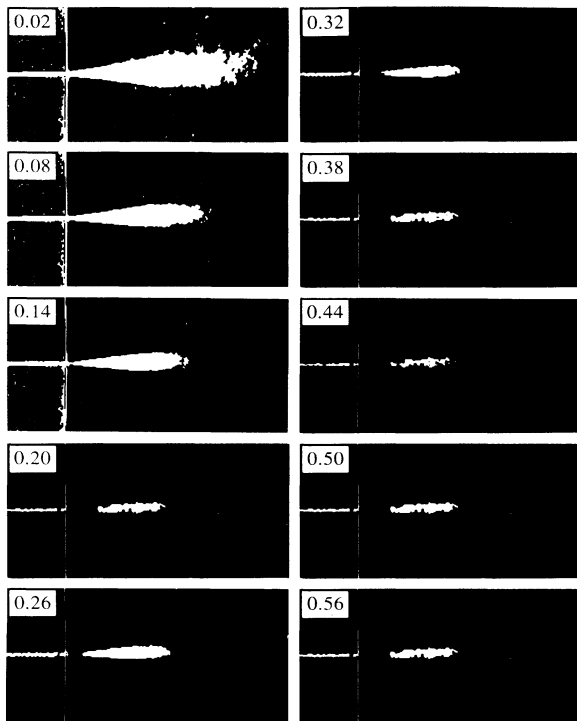


FIG. 3. The series of black and white displays that were traced to construct Fig. 2(d). For each of the ten diffusivity values (0.02, 0.08, ..., 0.50, 0.56  $\text{cm}^2\text{s}^{-1}$ ), the image was displayed so that pixels below the value were black and above it were white.

Fig. 2 is the line traced around a white area. Figure 4 shows contour maps of the diffusivity in the highest speed jet measured at three different echo times.

Using Eq. 1.123 of Davies,<sup>16</sup>  $v_0$  on the axis of the jet in Fig. 4 is  $1.2 \text{ m s}^{-1}$  10 cm from the nozzle. The distances  $|T_E v_0|$  upstream from that position (1.5, 1.7, and 2.9 cm for  $T_E$ 's of 13, 15, and 25 ms, respectively) are shown for each map in Fig. 4. None of the images had a  $\nabla D$  as high as  $0.56 \text{ cm}^2\text{s}^{-1}$  divided by a pixel width (0.125 cm), or  $4.48 \text{ cm s}^{-1}$ , and  $D\gamma^2 U(T_E)$  was less than 5 which means that in the 25-ms image,  $|T_E[D\gamma^2 U(T_E)]\nabla D| < 0.56 \text{ cm}$  or 4.5 pixel widths. The spatial misregistration from steady movement in the phase-encoding direction  $-v_{0y}\Delta t$  was less than

$$-(4.5 \text{ m s}^{-1})(\sin 10^\circ)(0.0056 \text{ s}) = -0.44 \text{ cm},$$

or the nozzle velocity times the sine of the jet angle times  $\Delta t$ . The signal-to-noise ratios ranged from 10 to 15 for diffusivities from 0.02 to  $0.7 \text{ cm}^2\text{s}^{-1}$ . Figure 5 shows the diffusivity image used to construct Fig. 4(b) displayed with a gray scale.

For pipe flow, the diffusivities upstream from any point are the same as at the point. The images were oriented so that the phase-encoding direction was in the direction of flow and  $|T_E[D\gamma^2 U(T_E)]\nabla D|$  was smaller than 3 pixel widths; for recording the average diffusivity in the pipe,

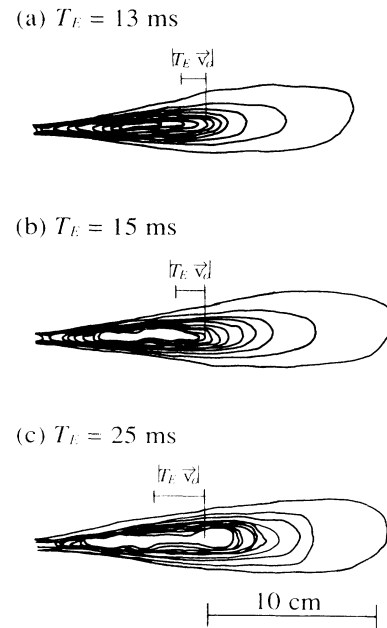


FIG. 4. Contour maps of the diffusivity in the highest speed jet measured with three different echo times. The Reynolds number is 18000. Diffusivities above  $0.56 \text{ cm}^2\text{s}^{-1}$  were not sufficiently resolved for drawing contour lines. A distance of  $|T_E v_0|$  upstream from a point 10 cm from the nozzle is shown for each map.

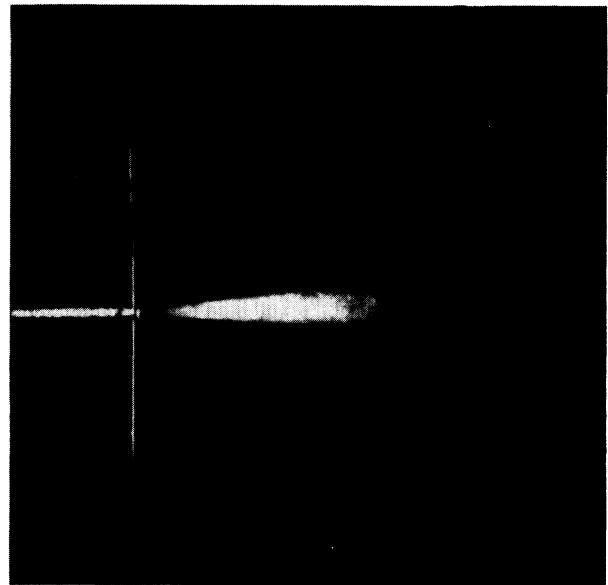


FIG. 5. The image used to construct Fig. 4(b) displayed with a gray scale. Pixel values below  $0.032 \text{ cm}^2\text{s}^{-1}$  are black, above  $0.480 \text{ cm}^2\text{s}^{-1}$  are white. Fourteen shades of gray are evenly distributed over the range  $0.032\text{--}0.480 \text{ cm}^2\text{s}^{-1}$ .

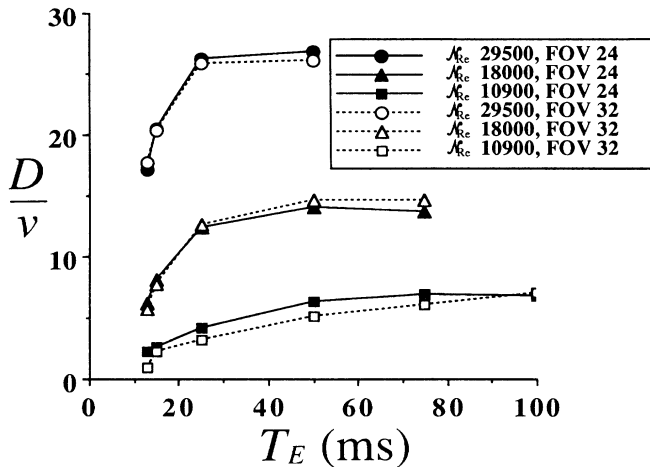


FIG. 6. Measured diffusivities vs echo time for pipe flow. The diffusivities are divided by the kinematic viscosity of water ( $\nu = \eta/\rho = 0.010 \text{ cm}^2 \text{ s}^{-1}$ , where  $\eta$  is the viscosity and  $\rho$  is the density of water at  $20^\circ\text{C}$ ) to produce a dimensionless diffusivity that can be compared to values measured in other fluids. Solid lines represent measurements with a 24-cm field of view (FOV), dashed lines represent measurements with a 32-cm field of view.

the bias was negligible. Figure 6 graphs the measured average diffusivity in the pipe at the three different flow rates using two different fields of view versus echo time. The diffusivities are divided by the kinematic viscosity of the water to provide a dimensionless number that can be compared with previous measurements in air. Figure 7

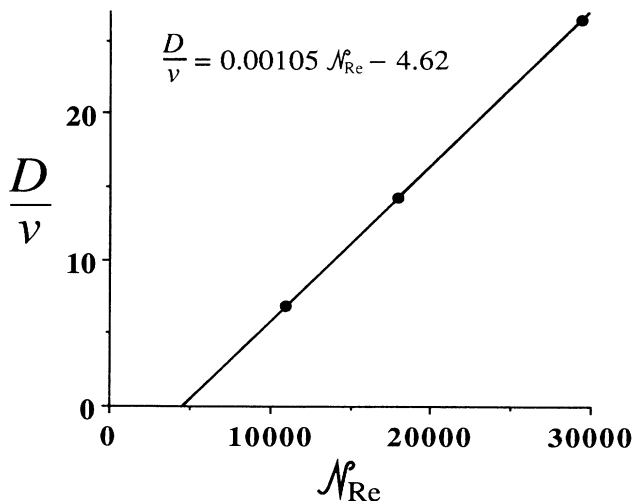


FIG. 7. Asymptotic dimensionless diffusivities from Fig. 6 are plotted vs Reynolds number. The Reynolds number for pipe flows is  $L\bar{v}/\nu$ , where  $L$  is the diameter of the pipe. The fact that the three data fall perfectly on a straight line to within three decimal places is fortuitous, as can be seen by their precision in Fig. 6.

shows the relationship between the asymptotic dimensionless diffusivities and the pipe flow Reynolds number.

#### IV. DISCUSSION

As Batchelor<sup>8</sup> predicted, the measured diffusivities in the pipe increased with short  $T_E$ 's but eventually reached an asymptote. Sheriff and O'Kane,<sup>17</sup> when measuring the diffusivity for nitrous oxide in turbulent air pipe flow, noticed that the measured diffusivity increased with distance downstream from their source but eventually reached an asymptote. Figure 8 graphs their data with two additional axes, one showing the time of flight from release of the nitrous oxide to the measurement of its concentration obtained by dividing the distance downstream by the average velocity  $\bar{v}$ , the other shows a dimensionless time scale  $t^*$  obtained by dividing the time of flight by  $L/\bar{v}$ , where  $L$  is the diameter of the pipe. Figure 9 shows the data from the present paper graphed with the dimensionless time scale. Sheriff and O'Kane's data and the present data all reach an asymptotic diffusivity at a  $t^*$  from 8 to 10. The relationship of  $D/\nu$  to the pipe flow Reynolds number appears to be a straight line (Fig. 7) as determined by previous studies.<sup>18</sup>

The asymptotic behavior of  $D$  and its linear relation to Reynolds number compare well with previous measurements; however, the values of  $D/\nu$  measured with

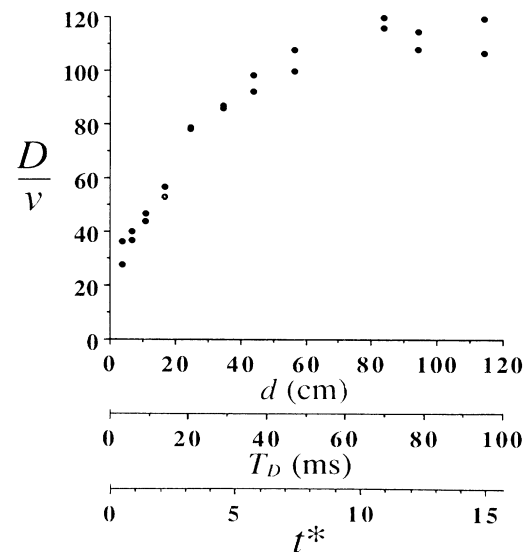


FIG. 8. The relationship of measured turbulent diffusivity of nitrous oxide in air pipe flow ( $N_{Re} = 60000$ ) with distance downstream  $d$  from source (from Ref. 17). Two additional axes are added: (1) diffusion time  $T_D$  between release and measurement ( $T_D = d/\bar{v}$ ) is analogous to echo time  $T_E$  in Fig. 6. (2)  $T_D$  is divided by  $L/\bar{v}$  to produce a dimensionless time  $t^* = T_D \bar{v}/L$ . Dynamically similar flows will have the same dimensionless time scale.

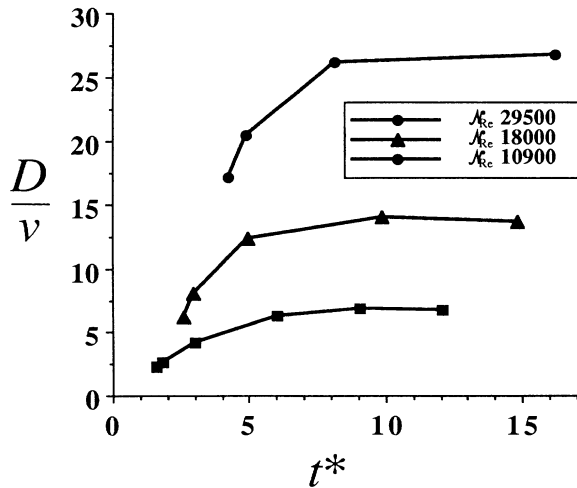


FIG. 9. Dimensionless diffusivities vs dimensionless time. The data are the same as the 24-cm field of view data in Fig. 6 but the echo time has been divided by  $L/\bar{v}$  to produce a dimensionless time  $t^* = T_E \bar{v}/L$ .

magnetic-resonance imaging are lower. Sheriff and O'Kane<sup>17</sup> compared measurements from four studies and they vary over a factor of 2 after being corrected for Reynolds number. The present values do not fall within their range; they are a factor of 2 lower than the center of the range of the previous studies. It is unlikely that magneto-hydrodynamic damping of the turbulence lowered the diffusivities, because the Hartman number of the flow  $[(\sigma B_0^2 a^2/\eta)^{0.5}]$ , where  $\sigma$  is the electrical conductivity of the fluid,  $a$  is the radius of the pipe, and  $\eta$  is the viscosity of the fluid] is only 0.05 and the Lundquist number  $[B_0 L \sigma (\mu/\rho)^{0.5}]$ , where  $\mu$  is the magnetic permeability and  $\rho$  is the density of the fluid] is only  $1.3 \times 10^{-8}$  (see Ref. 19). It also seems unlikely that the spatial scale (the size of the pixels) is too small for the motion to appear sufficiently random to be modeled as a diffusion because the diffusivities measured with a 32-cm field of view ( $1.25 \times 1.25 \text{ mm}^2$  pixels) are not greater than those measured with a 24-cm field of view ( $0.938 \times 0.938 \text{ mm}^2$  pixels) (Fig. 6). It is possible that the self-diffusion measured in this study is different from the mass diffusion measured in the previous studies; it is known that the measured turbulent diffusion of mass and momentum often differ by a factor of 2, especially for Reynolds numbers below 30 000 (Ref. 20). Also, the present measurements excludes molecular diffusion, whereas it was included in the previous measurements.

The diffusivities in the turbulent jet appear to increase more between a  $T_E$  of 13 and 15 ms than between 15 and 25 ms (Fig. 4), which indicates the asymptotic diffusivities may be approached shortly after 15 ms. The measurement at 15 ms is preferable to the one at 25 ms because of the greater spatial misrepresentation (bias) in the 25-ms image. One can see that the spatial misregistration is less than  $|T_E \mathbf{v}_0|$ , the upper bound for spatial misregistration,

by considering the diffusivity at the point 3.7 cm from the nozzle in the 15-ms image [Fig. 4(b)]. The velocity there is  $3.2 \text{ m s}^{-1}$  (Eq. 1.123 of Ref. 16) so the point  $|T_E \mathbf{v}_0|$  or 4.7 cm upstream lies in the pipe. From Fig. 7, the diffusivity in the pipe is about  $0.14 \text{ cm}^2 \text{ s}^{-1}$ , so the mapped diffusivity of 0.5 to  $0.56 \text{ cm}^2 \text{ s}^{-1}$  indicates the spatial misrepresentation is not as great as  $|T_E \mathbf{v}_0|$ . The actual bias could be approximated by comparing numerical solutions of (2) under a variety of diffusivity distributions to (3).

The technique presented in this paper has the advantage of measuring complicated distributions of turbulent diffusivity rapidly. The measurement time is short enough to aid in designing devices that make use of the turbulent diffusion of mass, heat, or momentum. While the diffusivities for these three quantities may be different from one another or self-diffusion by a multiplicative factor, an increase in the self-diffusion will indicate a similar increase in the others.

Because the diffusivities are stored in a computer file as a data matrix, they are in a convenient form for numerical simulations of diffusion. It should be possible to produce similar matrices of estimates of the components of  $\mathbf{v}_0$  using phase shifts produced by a different type of pulse sequence; it is possible to construct an image of the phase of  $m$  as well as its magnitude. Another possibility is measuring the components of anisotropic diffusivities by weighting  $U(T_E)$  heavily with one component, e.g., the frequency-encoding gradient, and making three sets of images of the same volume, each time frequency encoding a different direction.

The present method may have medical applications. Because blood often becomes turbulent in cardiovascular pathologies, it would be useful to have a measurement of the degree of turbulence to correlate with other measures of severity of disease. It is not practical to stop the blood flow of a patient to get an image of stationary blood; however, it would be possible to image a container of blood in the same field of view as the patient. Some error will be introduced in the calculation of  $D$  because the radio waves do not excite all regions equally; the pixel values for the container of blood may be different from those obtained if the stationary blood were inside the patient. By using a pulse sequence similar to Fig. 1, either the image will take a long time to collect, because of using a long repetition time, or the method will be less accurate because the moving blood will have received fewer previous excitations. A modification of a faster imaging technique<sup>21</sup> might be used to shorten the acquisition time.

#### ACKNOWLEDGMENTS

I thank E. O. Stejskal, Harold E. Layton, Stephen J. Riederer, Talin A. Tasciyan, Gary H. Glover, H. Cecil Charles, James R. MacFall, and Edward J. Shaughnessy for helpful discussions. I thank Harold E. Layton, Henry D. Sotsman, and James R. MacFall for comments on the manuscript. I thank the Department of Radiology at Duke University for supplies and the use of an imager.

## APPENDIX: ERROR ANALYSIS

### 1. Errors caused by assuming $D$ is a constant

Turbulent diffusivity decreases the magnitude of transverse magnetization in the presence of gradients in the magnetic field. Where there is a gradient in  $D$ , a gradient in  $m$  will develop. Magnetic moment can be brought to a point by net movement of fluid (convection) and turbulent diffusion driven by a gradient in  $m$ . We want to put bounds on the difference between the magnitude of the density of transverse magnetization  $m_{\text{true}}$  found at point  $p$  and time  $T_E$  in the case where  $D$  varies in space and the magnitude of the density of transverse magnetization  $m_{\text{assumed}}$  at  $p$  and  $T_E$  if  $D$  is constant. The difference in magnitude  $||m_{\text{true}}| - |m_{\text{assumed}}||$  cannot be greater as a result of convection than if the magnetization had developed for the entire  $T_E$  in the presence of the most different  $D$  found with  $|T_E \mathbf{v}_0|$  upstream of  $p$  rather than in the presence of  $D$  found at  $p$ .

The flux density of magnetic moment due to turbulent diffusion  $\mathbf{Q} = -D\nabla m$  can be interpreted as the moment density traveling at a net velocity:  $m\mathbf{v}_D = -D\nabla m$ . The gradient in  $m$  develops from the gradient in  $D$ ,  $\nabla m \cong -m\nabla D\gamma^2 U(t)$ , so  $m\mathbf{v}_D \cong Dm\nabla D\gamma^2 U(t)$  or  $m[D\gamma^2 U(t)]\nabla D$ . The velocity  $\mathbf{v}_D$  is  $\nabla D$  times the dimensionless factor  $D\gamma^2 U(t)$ . It starts at zero and increases with time. To be conservative, we can set the factor at  $D\gamma^2 U(T_E)$  when stating the bounds for the error:

$$i\gamma\mathbf{v}_0 \cdot \int_0^t \int_0^{t'} \mathbf{G}(t'') dt'' dt' = i\gamma \left[ v_{0x} \left[ t \int_0^t G_x(t') dt' - \int_0^t t' G_x(t') dt' \right] + v_{0y} \left[ t \int_0^t G_y(t') dt' - \int_0^t t' G_y(t') dt' \right] + v_{0z} \left[ t \int_0^t G_z(t') dt' - \int_0^t t' G_z(t') dt' \right] \right]$$

is zero throughout data collection.

The  $z$  term is in fact zero during data collection.<sup>14</sup> The  $y$  term is not zero during data collection. To form an image,  $\int_0^{T_E} G_y(t') dt'$  is nonzero for 255 of the 256 excitations. Because  $G_y$  is zero during data collection,  $t \int_0^t G_y(t') dt' - \int_0^t t' G_y(t') dt'$  cannot be zero. It can be minimized, however, by executing the  $y$  gradient as late as possible, maximizing  $\int_0^t t' G_y(t') dt'$ . In practice, the  $y$  gradient should end just before the  $x$  gradient is imposed for data collection. The error caused in the image by having

$$v_{0y} \left[ t \int_0^t G_y(t') dt' - \int_0^t t' G_y(t') dt' \right] \neq 0$$

is to displace objects in the  $y$  direction  $-v_{0y}\Delta t$  [where  $\Delta t$  is the time from the centroid of  $\int_0^{T_E} G_y(t') dt'$  to  $T_E$ ] from the point where they are at  $T_E$ . This spatial displacement must be added to our bounds for bias stated in the preceding section.

The  $x$  term is nonzero during data collection even though  $\int_0^t G_x(t') dt'$  and  $\int_0^t t' G_x(t') dt'$  cross zero at  $T_E$  (Ref. 14). If there is a  $\mathbf{v}_0$  component in the  $x$  direction, the phase of  $M$  changes in time (recall  $\alpha$  is timelike) and

The difference  $||m_{\text{true}}| - |m_{\text{assumed}}||$  cannot be greater as a result of diffusion along a gradient in  $m$  caused by a gradient in  $D$  than if the magnetization had developed for the entire  $T_E$  at the most different  $D$  found within  $|T_E[D\gamma^2 U(T_E)]\nabla D|$  of  $p$  in the direction of either  $\pm\nabla D$ . In general, the factor  $D\gamma^2 U(T_E)$  will not be greater than 4.6 because, from (3), the magnitude of the moment density will be less than  $\frac{1}{100}$  of its value for stationary fluid  $m_m = m_s e^{-D\gamma^2 U(T_E)} = m_s e^{-4.6} = \frac{1}{100} m_s$  and, from (4), the measurement technique will not discriminate well between higher  $D$ 's. In this study, the factor  $D\gamma^2 U(T_E)$  was below 5.

We can summarize the bias as a lack of spatial resolution by stating: A diffusivity at a point in an image represents a diffusivity somewhere in the region within  $|T_E[D\gamma^2 U(T_E)]\nabla D|$  in the direction of either  $\pm\nabla D$ , and within  $|T_E \mathbf{v}_0|$  upstream.

There will be some diffusive transport of the phase of transverse magnetization within the distance  $|T_E[D\gamma^2 U(T_E)]\nabla D|$ ; however, as we shall see in the next section which deals with the convective transport of phase, errors in phase of this type will not introduce bias in measuring  $D$  but will decrease the signal-to-noise ratio in parts of the image.

### 2. Errors caused by assuming $\int_0^t \int_0^{t'} \mathbf{G}(t'') dt'' dt'$ is zero during data collection

The method assumes

an imaginary component will be introduced into the discrete inverse Fourier transform [the sum over  $j$  in (7)] of  $\int_{-\infty}^{\infty} e^{-ias_x} M ds_x$ . The possible errors in phase and magnitude will be summed over  $k$  in (7) and cause errors in  $f$  and thus in the image  $|f|$ . The phase errors do not change with each of the 256 excitations in proportion to  $\beta_k$ . They will not result in a spatial displacement in  $y$  but will cause noise to be spread in the image in the  $y$  direction. Noise can be measured after the imaging is complete.

The possible errors in the *magnitude* of the discrete inverse Fourier transform of  $\int_{-\infty}^{\infty} e^{-ias_x} M ds_x$  are of greater concern because they could introduce bias into the measurement of  $D$ . The bias can be estimated by taking the discrete inverse Fourier transform of  $\int_{-\infty}^{\infty} e^{-ias_x} M ds_x$  for different hypothetical velocity distributions. Figure 10 shows four examples, columns I–IV. The top row of graphs gives the velocity distribution for each example. The middle row gives the magnitude of the inverse fast Fourier transform of  $\int_{-\infty}^{\infty} e^{-ias_x} M ds_x$ ; the bottom row gives the phase. For stationary material (column I), we assume  $M = 1 + 0i$  for

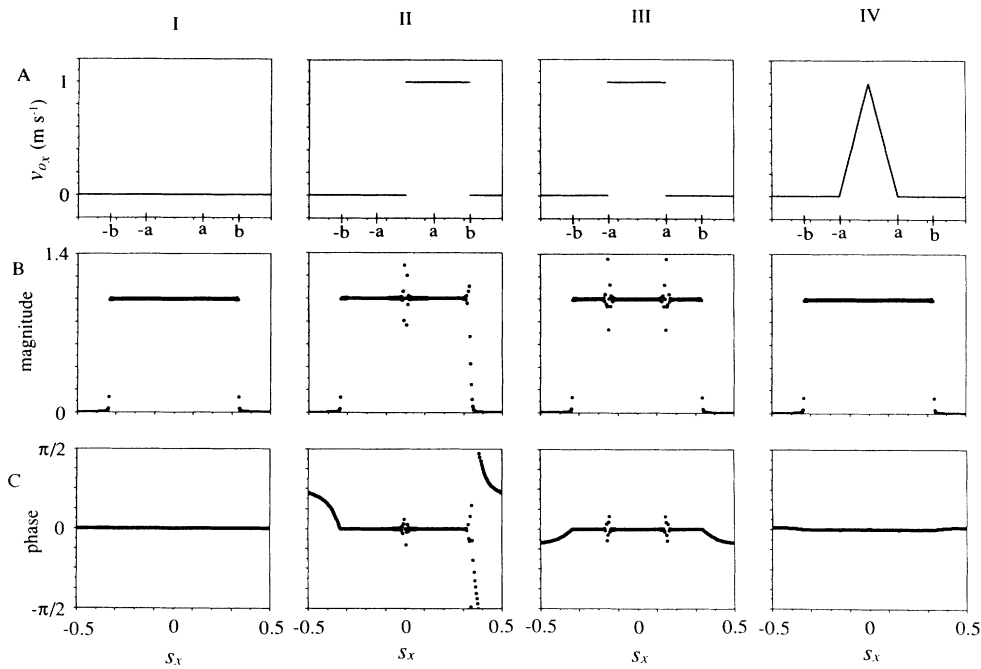


FIG. 10. Image errors from net steady movement in the frequency-encoding direction. Row *A* shows four steady velocity distributions (columns I–IV). Rows *B* and *C* show the magnitude and phase, respectively, of the inverse fast Fourier transform of  $\int_{-\infty}^{\infty} e^{-i\alpha s_x} M ds_x$ . The magnitude is like a one-dimensional image. Departures from the magnitude in column I, row *B* would introduce bias in the measurement of *D*. Departures from the phase in column I, row *C* would lower the signal-to-noise ratio in regions of the image in the phase-encoding direction of the departure. For stationary fluid, *M* is  $1+0i$  between  $-b$  and  $b$  and is  $0+0i$  elsewhere. Where there is net steady fluid movement in the frequency-encoding direction, *M* contains the factor  $e^{iu\alpha^2}$ , where  $u = v_{0x}/2\gamma G_x \xi^2$ .

$s_x$  between  $-b$  and  $b$  and  $M=0+0i$  elsewhere. Then, the signal is

$$S(t) = S(\alpha) = e^{-i\omega_0(t-T_E)} \int_{-b}^b e^{-i\alpha s_x} ds_x = e^{-i\omega_0(t-T_E)} \frac{2 \sin(b\alpha)}{\alpha} \tag{A1}$$

Where there is a net movement of fluid in the  $x$  direction, *M* obtains a factor  $e^{iu\alpha^2}$ , where  $u = v_{0x}/2\gamma G_x \xi^2$ , from the fourth term of the exponent of (3). The signal can be obtained for simple velocity distributions after some lengthy algebraic manipulations with trigonometry theorems. If the right half of the material is moving (column II) the signal is

$$S(t) = S(\alpha) = e^{-i\omega_0(t-T_E)} \int_{-b}^b \left[ e^{-i\alpha s_x} \times \begin{cases} e^{iu\alpha^2}, & 0 \leq s_x \leq b \\ 1 & \text{otherwise} \end{cases} \right] ds_x = e^{-i\omega_0(t-T_E)} \left[ \frac{2 \sin(b\alpha)}{\alpha} \cos^2 \left[ \frac{u\alpha^2}{2} \right] + \frac{2 \sin^2 \left[ \frac{b\alpha}{2} \right]}{\alpha} \sin(u\alpha^2) + i \frac{2 \sin(b\alpha)}{\alpha} \frac{\sin(u\alpha^2)}{2} + \frac{2 \sin^2 \left[ \frac{b\alpha}{2} \right]}{\alpha} 2 \sin^2 \left[ \frac{u\alpha^2}{2} \right] \right], \tag{A2}$$

for a central region of the material moving (column III) the signal is

$$\begin{aligned}
 S(t) = S(\alpha) &= e^{-i\omega_0(t-T_E)} \int_{-b}^b \left[ e^{-ias_x} \times \begin{cases} e^{iu\alpha^2}, & |s_x| \leq a \\ 1 & \text{otherwise} \end{cases} \right] ds_x \\
 &= e^{-i\omega_0(t-T_E)} \left[ \frac{2}{\alpha} [\sin(b\alpha) - \sin(a\alpha)] + \frac{2}{\alpha} \cos(u\alpha^2) \sin(a\alpha) + i \frac{2}{\alpha} \sin(u\alpha^2) \sin(a\alpha) \right], \quad (A3)
 \end{aligned}$$

for the velocity distribution in Fig. 10, column IV, row *A* the signal is

$$\begin{aligned}
 S(t) = S(\alpha) &= e^{-i\omega_0(t-T_E)} \int_{-b}^b \left[ e^{-ias_x} \times \begin{cases} e^{i(1-|s/a|\alpha^2)/q}, & |s_x| \leq a \\ 1 & \text{otherwise} \end{cases} \right] ds_x \\
 &= e^{-i\omega_0(t-T_E)} \left\{ \frac{2}{\alpha} [\sin(b\alpha) - \sin(a\alpha)] + \frac{2qa}{\alpha(q^2a^2 - \alpha^2)} \left[ qa \sin(a\alpha) - \alpha \sin\left(\frac{\alpha^2}{q}\right) \right] \right. \\
 &\quad \left. + i \frac{2qa}{(q^2a^2 - \alpha^2)} \left[ \cos\left(\frac{\alpha^2}{q}\right) - \cos(a\alpha) \right] \right\}, \quad (A4)
 \end{aligned}$$

where  $q = 2\gamma G_x \xi^2$ .

Figure 10, column I, row *B* shows Gibbs's phenomenon at discontinuities of  $M$  characteristic of discrete inverse Fourier transforms. Figure 10, column II, row *B* shows Gibbs's phenomenon is worse at discontinuities of the velocity distribution. Figure 10, column II, row *B*, and column III, row *B*, show Gibbs's phenomenon is worse when the velocity distribution is discontinuous within the material rather than at the edge and that the error for symmetrical velocity distributions is similar to that for asymmetrical ones. Figure 10, column IV, row *A* has a more realistic continuous velocity distribution and does not show errors in magnitude

greater than those for stationary material even though the velocity distribution is not smooth. Because velocity distributions in fluids are continuous, Fig. 10, column IV, row *B* indicates that assuming

$$v_{0x} \left[ t \int_0^t G_x(t') dt' - \int_0^t t' G_x(t') dt' \right] = 0$$

throughout data collection will not introduce bias in measuring  $D$ . In fact, because the phase errors in column IV, row *C* are also small, the noise introduced in areas of the image in the  $\pm y$  direction of where  $v_0$  has an  $x$  component may be small as well.

<sup>1</sup>H. Y. Carr and E. M. Purcell, *Phys. Rev.* **94**, 630 (1954); E. O. Stejskal and J. E. Tanner, *J. Chem. Phys.* **42**, 288 (1965); E. O. Stejskal *ibid.* **43**, 3597 (1965).

<sup>2</sup>C. B. Ahn, S. Y. Lee, O. Nalcioglu, and Z. H. Cho, *Med. Phys.* **13**, 789 (1986); D. Le Bihan, *Magn. Reson. Med.* **7**, 346 (1988); K-D. Merboldt, W. Hänicke, and J. Frahm, *J. Magn. Reson.* **64**, 479 (1985); D. G. Taylor and M. C. Bushell, *Phys. Med. Biol.* **30**, 345 (1985); G. E. Wesbey, M. E. Moseley, and R. E. Ehman, *Invest. Radiol.* **19**, 491 (1984).

<sup>3</sup>This paper assumes the turbulence is isotropic ( $D$  is not a function of direction). It may be possible to measure anisotropic diffusivities with magnetic resonance.

<sup>4</sup>A. Fick, *Ann. Phys. Chem.* **94**, 59 (1855); G. I. Taylor, *Philos. Trans.* **215**, 1 (1915).

<sup>5</sup>G. T. Csanady, *Turbulent Diffusion in the Environment* (Reidel, Boston, 1972); F. N. Frenkiel and R. E. Munn, *Turbulent Diffusion in Environmental Pollution: Proceedings of a Symposium held at Charlottesville, Virginia, April 8-14, 1973* (Academic, New York, 1974).

<sup>6</sup>W. H. Bossert and E. O. Wilson, *J. Theoret. Biol.* **5**, 443 (1963).

<sup>7</sup>T. K. Sherwood, R. L. Pigford, and C. R. Wilke, *Mass Transfer* (McGraw-Hill, New York, 1975).

<sup>8</sup>G. K. Batchelor, *Austral. J. Sci. Res.* **2**, 437 (1949).

<sup>9</sup>G. K. Batchelor, *An Introduction to Fluid Dynamics* (Cambridge University Press, Cambridge, England, 1967).

<sup>10</sup>F. Bloch, *Phys. Rev.* **70**, 460 (1946); H. C. Torrey, *ibid.* **104**, 563 (1956); E. O. Stejskal, *J. Chem. Phys.* **43**, 3597 (1965).

<sup>11</sup>F. Bloch, *Phys. Rev.* **70**, 460 (1946).

<sup>12</sup>E. L. Hahn, *Phys. Rev.* **80**, 580 (1950).

<sup>13</sup>E. O. Stejskal, *J. Chem. Phys.* **43**, 3597 (1965).

<sup>14</sup>E. M. Haacke and G. W. Lenz, *Amer. J. Radiol.* **148**, 1251 (1987).

<sup>15</sup>W. A. Edelstein, J. M. S. Hutchison, G. Johnson, and T. Redpath, *Phys. Med. Biol.* **25**, 751 (1980).

<sup>16</sup>J. T. Davies, *Turbulence Phenomena: An Introduction to the Eddy Transfer of Momentum, Mass, and Heat, Particularly at Interfaces* (Academic, New York, 1972).

<sup>17</sup>N. Sheriff and D. J. O'Kane, *Int. J. Heat Mass Trans.* **14**, 697 (1971).

<sup>18</sup>N. Sheriff and D. J. O'Kane, *Int. J. Heat Mass Trans.* **14**, 697 (1971); A. Quarmby and R. K. Anand, *J. Fluid Mech.* **38**, 433 (1969).

<sup>19</sup>G. W. Sutton and A. Sherman, *Engineering Magnetohydrodynamics* (McGraw-Hill, New York, 1965).

<sup>20</sup>A. Quarmby and R. K. Anand, *J. Fluid Mech.* **38**, 433 (1969).

<sup>21</sup>D. Le Bihan, *Magn. Reson. Med.* **7**, 346 (1988).

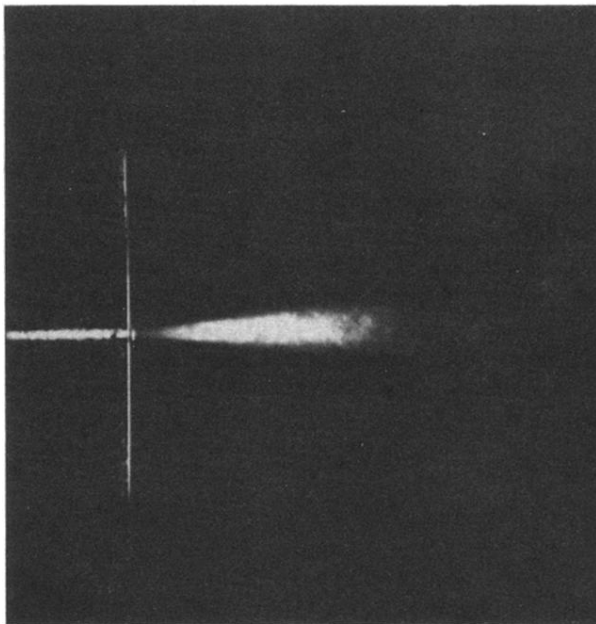


FIG. 5. The image used to construct Fig. 4(b) displayed with a gray scale. Pixel values below  $0.032 \text{ cm}^2 \text{ s}^{-1}$  are black, above  $0.480 \text{ cm}^2 \text{ s}^{-1}$  are white. Fourteen shades of gray are evenly distributed over the range  $0.032\text{--}0.480 \text{ cm}^2 \text{ s}^{-1}$ .